

Coupled Mechanical and Electrochemical Analyses of Three-Dimensional Reconstructed LiFePO_4 by Focused Ion Beam/Scanning Electron Microscopy in Lithium-Ion Batteries

Sangwook Kim

Mechanical and Aerospace
Engineering Department,
North Carolina State University,
R3311 Engineering Building 3,
Campus Box 7910 911,
911 Oval Drive,
Raleigh, NC 27695
e-mail: skim49@ncsu.edu

Hongjiang Chen

Mechanical and Aerospace
Engineering Department,
North Carolina State University,
R3311 Engineering Building 3,
Campus Box 7910 911,
911 Oval Drive,
Raleigh, NC 27695
e-mail: hchen30@ncsu.edu

Hsiao-Ying Shadow Huang¹

Mechanical and Aerospace
Engineering Department,
North Carolina State University,
R3158 Engineering Building 3,
Campus Box 7910 911,
911 Oval Drive,
Raleigh, NC 27695
e-mail: hshuang@ncsu.edu

Limited lifetime and performance degradation in lithium ion batteries in electrical vehicles and power tools is still a challenging obstacle which results from various inter-related processes, especially under specific conditions such as higher discharging rates (C-rates) and longer cycles. To elucidate these problems, it is very important to analyze electrochemical degradation from a mechanical stress point of view. Specifically, the goal of this study is to investigate diffusion-induced stresses and electrochemical degradation in three-dimensional (3D) reconstructed LiFePO_4 . We generate a reconstructed microstructure by using a stack of focused ion beam-scanning electron microscopy (FIB/SEM) images combined with an electrolyte domain. Our previous two-dimensional (2D) finite element model is further improved to a 3D multiphysics one, which incorporates both electrochemical and mechanical analyses. From our electrochemistry model, we observe 95.6% and 88.3% capacity fade at 1.2 C and 2 C, respectively. To investigate this electrochemical degradation, we present concentration distributions and von Mises stress distributions across the cathode with respect to the depth of discharge (DoD). Moreover, electrochemical degradation factors such as total polarization and over-potential are also investigated under different C-rates. Further, higher total polarization is observed at the end of discharging, as well as at the early stage of discharging. It is also confirmed that lithium intercalation at the electrode-electrolyte interface causes higher over-potential at specific DoDs. At the region near the separator, a higher concentration gradient and over-potential are observed. We note that higher over-potential occurs on the surface of electrode, and the resulting concentration gradient and mechanical stresses are observed in the same regions. Furthermore, mechanical stress variations under different C-rates are quantified during the discharging process. With these coupled mechanical and electrochemical analyses, the results of this study may be helpful for detecting particle crack initiation. [DOI: 10.1115/1.4040760]

1 Introduction

Limited lifetime and performance degradation in lithium ion batteries in electrical vehicles and power tools resulting from various interrelated processes is still a challenging obstacle [1]. Typically, these phenomena are more serious under specific conditions such as at higher discharging rates (C-rates) and with longer cycling life [2]. One of the main reasons for battery degradation is the large mechanical stress resulting from volume expansion (or contraction) during the (dis)charging processes. It is well known that stress-induced fractures degrade the performance of lithium ion cells, as evidenced by the observation of fractured surfaces in postmortem analysis of batteries [3]. Moreover, Xu and Zhao [4] reported that the insertion of lithium is blocked by the high local compressive stress, and finally, results in significant reduction of the effective capacity. Lu et al. [5] also confirmed by theoretical and experimental analyses that mechanical stress plays an important role in voltage hysteresis in lithium ion batteries. It is,

therefore, very important to analyze electrochemical degradation due to mechanical stresses.

As LiFePO_4 cells are discharged, both lithium intercalation at the cathode–electrolyte interface and diffusion inside the cathode can result in diffusion-induced stress. Early stage studies analyzed diffusion-induced stresses in cathode materials based on simple geometries such as spheres, spheroids, cylinders, and disks by using Newman’s pseudo-two-dimensional (2D) model, while recognizing that stress development has a major impact on the performance of lithium ion batteries. However, there were still limitations when simple geometries were used because they failed to predict the phenomena relating to the inhomogeneous natures of the electrode microstructures [6]. Currently, more studies are focusing on realistic microstructures of electrodes to investigate diffusion-induced stress. Mendoza et al. [6] investigated the mechanical and electrochemical responses of a LiCoO_2 cathode during charging. They reported mechanisms of stress generation and the effect of charge rate on capacity fade. Stress generation in LiCoO_2 [6], LiMn_2O_4 [7], and nickel-manganese-cobalt [8] has also been investigated using realistic microstructures.

Three-dimensional (3D) characterization methods such as focused ion beam-scanning electron microscopy (FIB-SEM) and

¹Corresponding author.

Manuscript received April 9, 2018; final manuscript received June 26, 2018; published online August 6, 2018. Assoc. Editor: Partha P. Mukherjee.

X-ray computed micro/nanotomography have been commonly used to quantify electrode microstructural parameters including grain size, phase volume, surface area, phase connectivity, and tortuosity [9]. Ender et al. [10] first presented a 3D reconstructed LiFePO₄ model obtained by FIB/SEM tomography. Based on the reconstructed figures, they analyzed microstructural features such as active surface areas, particle size distribution, porosity, and tortuosity of the pore phase for both LiFePO₄ and carbon black. Moreover, detailed structural degradation of LiFePO₄ was investigated by using low voltage FIB/SEM [11]. Biton et al. developed a new methodology via contrast enhancement for 3D imaging of LiFePO₄ [9]. Nanoscale X-ray computed tomography data have been utilized for a 3D microstructure of LiFePO₄ to investigate the distribution of lithium ion concentration inside LiFePO₄ during discharging [12]. Kashkooli et al. [12] demonstrated that their electrochemical results from the reconstructed geometry were in good agreement with experimental measurements. However, we could only uncover one published study focusing on investigating stress generation within the 2D microstructure of LiFePO₄ [3]. Nevertheless, a complete study of the 3D electrode microstructure is required to better understand the coupled mechanical and electrochemical effects in lithium ion batteries.

A multiscale multiphysics finite element model consisting of one-dimensional electrochemistry, 2D axis symmetry heat generation, 2D mass transport, and 2D solid mechanics was previously established to investigate thermal- and diffusion-induced stresses in the reconstructed porous microstructures of commercial LiFePO₄ batteries [3]. Specifically, with the 2D model, we could investigate the effects of lithium ion concentration and stress in the cathode with complicated geometry such as at concave and/or convex corners and particle connecting areas. Moreover, it was confirmed that a strong relationship existed between mechanical stresses and capacity loss in lithium ion batteries. However, our previous model had several limitations, such as one-dimensional electrochemistry and the assumption that 2D solid mechanics behave exactly the same throughout the depth of the battery (i.e., along the *z*-axis). We realized that a three-dimensional fully coupled finite element model is essential to better study performance degradation in lithium ion batteries.

The current study is intended to demonstrate a methodology for using FIB/SEM to generate a 3D reconstructed microstructure through the conjunction of simulations for electrochemistry and solid mechanics to better understand the battery system. This paper presents an improved 3D fully coupled electrochemical-mechanical model, which is crucial for establishing the relationship between electrochemical performance and mechanical stresses. Specifically, our primary focus was on the effects of complicated structure on mechanical stresses and the prediction of particle crack initiation in LiFePO₄ cells.

2 Methods

2.1 Construction of the Microstructure. The LiFePO₄ sample for microscopy was prepared according to the study published by Kim and Huang [3]. Briefly, FIB/SEM imaging was carried out using FEI Quanta 3D FEG (FIB-SEM) at the NC State Analytical Instrument Facility (AIF, Raleigh, NC). As shown in Fig. 1(a), the sample stage was tilted to 52 deg and the FIB was perpendicular to the sample, which allowed cross-sectional micromilling. To focus on the region of interest, each side of the region of interest was milled by the FIB. For more detailed particle configuration, a sector of $2.5 \times 2.5 \mu\text{m}^2$ with higher magnification ($>15,000\times$) was used. The pixel size of the scanning electron microscopy (SEM) images was 4.06 nm. Since a polyvinylidene difluoride (PVDF) binder was likely to be an ultrathin layer below the resolution, which made it difficult to distinguish from the LiFePO₄ cathode using SEM [9], carbon black and the PVDF binder were not considered in this study. Figure 1(b) presents a stack of over 50 SEM images. The smoothing and edge finding processes in the

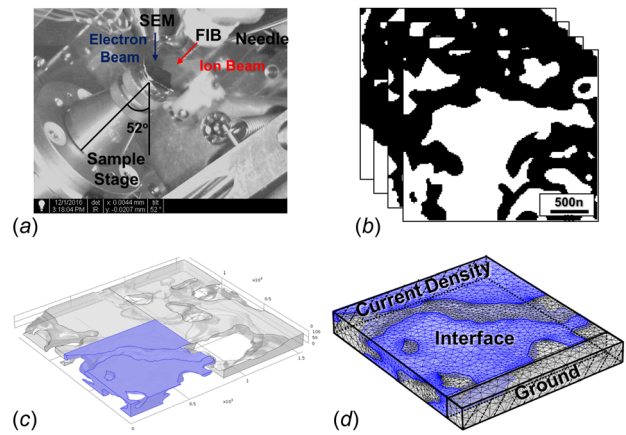


Fig. 1 (a) Experimental setup for FIB-SEM, (b) a stack of 2D images, (c) 3D reconstructed microstructure of LiFePO₄, and (d) final microstructure and mesh in COMSOL MULTIPHYSICS

ImageJ analysis software (National Institute of Health, Bethesda, MD) were conducted to determine the boundary between the electrolyte and the electrode. Moreover, binary images were produced based on a threshold prior to the 3D reconstruction process. Based on the set of cross-sectional images, a 3D microstructure was also generated in ImageJ and exported in Standard Tessellation Language (STL) format, which allows the files to be imported into COMSOL MULTIPHYSICS (Fig. 1(c)). Since a 3D microstructure with $1.5 \times 1.5 \times 0.1 \mu\text{m}^3$ was computationally expensive to reduce the computation time, the geometry was partitioned to a final size of $0.8 \times 0.8 \times 0.1 \mu\text{m}^3$, which was shown in shaded region in Fig. 1(c). The imported 3D microstructure was combined with a 100 nm thick electrolyte domain. Current density was applied to the left side of the half-cell domain (i.e., the current collector) and the ground was set on the right side of the electrolyte (Fig. 1(d)). The mesh was generated via COMSOL MULTIPHYSICS and the mesh size was optimized using a standard finite element model procedure based on convergence [6]. The maximal and minimal sizes of the generated mesh were 9.16 nm and 1.65 nm, respectively.

2.2 Mathematical Model. This section summarizes the equations for electrochemistry and solid mechanics for both the electrodes and electrolyte, including elastic strain and diffusion induced strain during repeated charging–discharging cycles (Table 1). Diffusion induced strain was observed to be over an order of magnitude larger than thermal strain based on our previous work [3]. Thus, in the current study, we only focused on diffusion induced strain in cathode particles. To represent phase transformation between LiFePO₄ and FePO₄, concentration-dependent material properties were incorporated into the material property [K], such as the Poisson's ratio and Young's modulus described in Table 2, and were defined as $K(x) = \text{DoD}[K]^{\text{LiFePO}_4} + (1 - \text{DoD})[K]^{\text{FePO}_4}$. DoD was calculated by the following equation:

$$\text{DoD} = \frac{\sum_{i=1}^n C_i V_i}{\sum_{i=1}^n C_{\max} V_i} \quad (1)$$

where *V* and *n* indicated the volume of the 3D ten-node tetrahedral mesh and the total number of meshes, respectively. *C*_{max} indicates the maximum concentration at the cathode [15].

Total polarization and over potential were calculated to quantify electrochemical battery degradation. The total polarization was defined as the difference between the open circuit voltage and the cell voltage as described by the following equation:

Table 1 Summary of equations in this computational model

Analysis	Type	Description	Equations	#
Electro-chemistry	Cathode	Charge balance	$\nabla \cdot (-\sigma_s \nabla \phi_s) = 0$	a
		Mass transport	$J_s = -D_s \nabla C_s$	b
	Electrolyte	Charge balance	$\nabla \cdot \left(-\sigma_l \nabla \phi_l + \frac{2\sigma_l RT}{F} (1 + \frac{\partial \ln f}{\partial \ln c_l}) (1 - t_+) \nabla \ln c_l \right) = 0$	c
		Mass transport	$J_l = -D_l \nabla c_l + \frac{i_l t_+}{F}$	d
	Interface	Electro-chemical kinetics	$i_{loc} = i_0 \left(\exp\left(\frac{\alpha_a F \eta}{RT}\right) - \exp\left(\frac{-\alpha_c F \eta}{RT}\right) \right)$	e
			$i_0 = F(k_c)^{z_a} (k_a)^{z_c} (C_{s,max} - C_s)^{z_a} (C_s)^{z_c} \left(\frac{C_l}{C_{l,ref}}\right)^{z_a}$	f
Solid mechanics	Total strain		$\varepsilon_T = \varepsilon_{el} + \varepsilon_{diff}$	g
			$\varepsilon_{ij}^{el} = \frac{1}{E} [(1 + \nu)\tau_{ij} - \nu\tau_{kk}\delta_{ij}]$	h
			$\varepsilon_{ij}^{diff} = \beta \Delta C \delta_{ij}$	i

Table 2 List of material properties used in this work

		Electrolyte	Cathode	Unit
Electro-chemistry	Initial concentration (c_0)	2000 ^a	2000 ^a	mol/m ³
	Maximum concentration (C_{max})		22,800	mol/m ³
	Diffusion coefficient (D)	3×10^{-10}	7×10^{-18}	m ² /s
Solid mechanics	Young's modulus	LiFePO ₄	117.8	GPa
		FePO ₄	108.2	GPa
	Poisson's ratio	LiFePO ₄	0.3	
		FePO ₄	0.23	

^aEstimated value [13,14].

$$\text{total polarization} = E_{OCV,cell} - E_{cell}$$

where $E_{OCV,cell}$ and E_{cell} describe the open circuit voltage and cell voltage, respectively.

Also, overpotential on the interface between the electrolyte and the electrode was calculated by the following equation:

$$\eta = \phi_s - \phi_l - E_{eq} \quad (2)$$

where ϕ_s , ϕ_l , and E_{eq} were the electrode local potential, electrolyte local potential, and equilibrium potential, respectively.

To quantify the stress, the von Mises stress was chosen, which is typically used for metals as a scalar indicator of the overall stress state and to provide a failure criterion [3]

$$\sigma_{VM} = \sqrt{\frac{(\sigma_1 - \sigma_2)^2 + (\sigma_2 - \sigma_3)^2 + (\sigma_3 - \sigma_1)^2}{2}} \quad (3)$$

where σ_1 , σ_2 , and σ_3 are principal stresses.

2.3 Model Parameters. Table 2 summarizes the material properties used in this model. From Zhu et al. [16], the orientation of the crystalline and grain microstructures were distributed randomly so that macroscopic elastic properties were almost equal in all directions. Thus, by adopting this same idea, isotropic material properties for solid mechanics were used in this study. Moreover, current density was set as -24 A/m^2 , -50 A/m^2 , and -70 A/m^2 to represent 0.6 C, 1.2 C, and 2 C, respectively, and were applied on the left side of the electrode (Fig. 1(d)).

3 Results

Figure 2 shows the electrical potential curves for the LiFePO₄ during the discharging process at three different C-rates. The upper and lower potential limits were 3.8 V and 2.0 V,

respectively. The plateau during the discharging process was observed around 3.4 V. Total discharging times for 0.6 C, 1.2 C, and 2 C were 6000 s, 2868 s, and 1589 s, respectively. To compare the predicted capacity of the models at different C-rates, a 100% capacity was used for the 0.6 C model for relative comparison. We observed that the capacity of the cathode under 0.6 C, 1.2 C, and 2 C were 100%, 95.6%, and 88.3%, respectively. We hypothesized that the capacity fade was caused by higher stress in the electrode based on our previous work, thus we further investigated the electrochemical and mechanical behaviors in the half cell system.

Because the lithium ion concentration gradient induces mismatched strains and generates mechanical stresses [17], we investigated the concentration distribution in the microstructure of

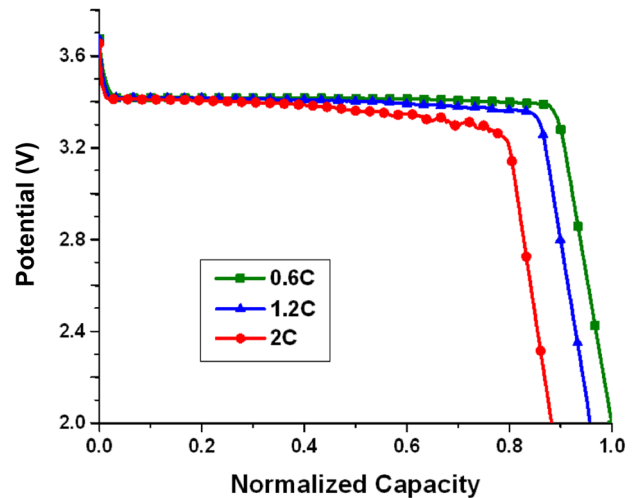


Fig. 2 Potential change during the discharging process under different C-rates

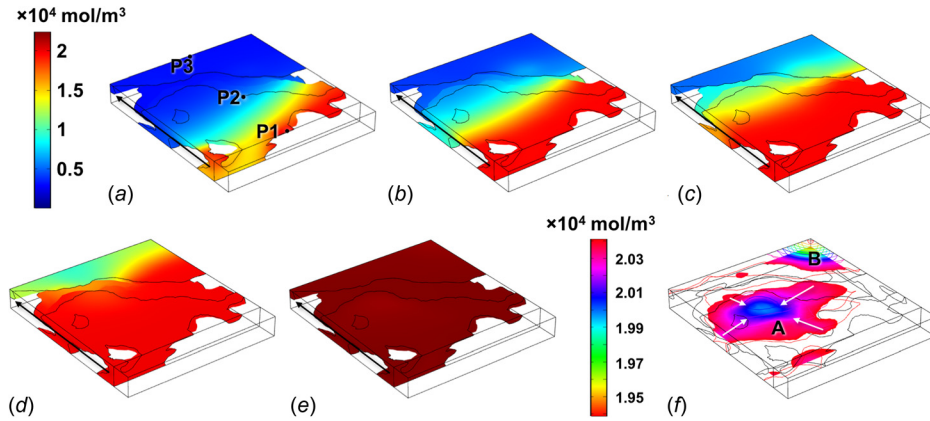


Fig. 3 Concentration distribution at 0.6 C at (a) 1200 s, (b) 2400 s, (c) 3600 s, (d) 4800 s, (e) 5400 s (color legend), and (f) cross-sectional contour plot at 5400 s in cyclic legend

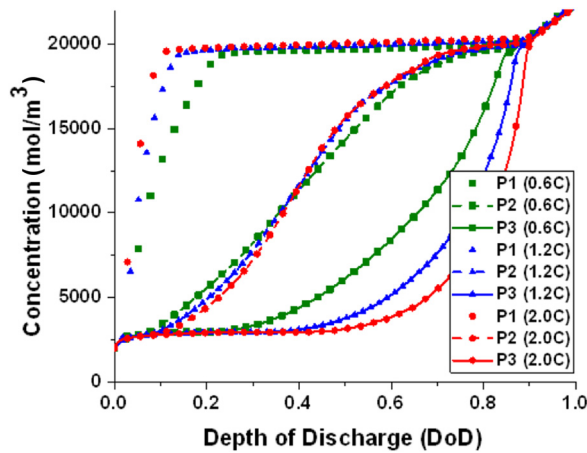


Fig. 4 Concentration variation at three different points, P_1 , P_2 , and P_3 (marked in Fig. 3) under various C -rates (i.e., 0.6 C, 1.2 C, and 2.0 C)

LiFePO_4 . In Fig. 3, P_1 , P_2 , and P_3 indicate the region near the separator, at the middle of the cathode, and the region near the current collector, respectively. As discharge proceeded, the cathode was lithiated along the direction from the separator to the current collector (as shown by a black arrow in Figs. 3(a)–3(e)). At 5400 s (i.e., at the depth of discharge (DoD) of 0.9 at 0.6 C), the surface of the electrode was fully saturated (Fig. 3(e)). Even though the cathode surface was fully saturated, the region inside the particle was not saturated, as shown in Fig. 3(f). The particle in the middle

of the cathode (marked as A) has a higher concentration than the particle near the current collector (marked as B) (Fig. 3(f)). Moreover, we could also confirm that lithium ions diffused from outside toward the inside, as indicated by the white arrow.

The lithium ion concentration variations, ranging from 2000 mol/m^3 to $22,800 \text{ mol/m}^3$ under the three C -rates shown in Fig. 4, had demonstrated drastic differences upon discharging in the region near the separator (P_1), as compared to the one near the current collector (P_3). In this study, we used the slopes of the curves in Fig. 4 to present the concentration gradient. As many studies have demonstrated that a higher lithium ion concentration gradient would result in higher stress [2,3,18,19], our results in Fig. 4 may be used to explain why cracks were generally observed near the separator in cathode materials [13]. It was observed that higher C -rate resulted in higher concentration gradients at both P_1 and P_3 , whereas lithium-ion concentration changed gradually at lower C -rate. By comparing P_1 , P_2 , and P_3 under each C -rate, lithium ion concentration in the region near the separator increased and saturated in the early stages of discharging, whereas lithium ion concentration at the region near the current collector increased and saturated at the end of discharging. Interestingly, different phenomena were observed at P_2 : before $\text{DoD} = 0.37$ (Fig. 4), the concentration gradient at lower C -rate was steeper than that at higher C -rate. After $\text{DoD} = 0.37$, this trend was reversed. In spite of different C -rates, each DoD moves the same amount of lithium across the electrode. In other words, only a small portion of the electrode had a relatively higher lithium ion fraction at higher C -rate. On the other hand, at lower C -rates, a larger portion of the electrode was discharged with a relative lower lithium ion fraction. Thus, we concluded that at the same DoD, higher C -rate could possibly result in a more inhomogeneous lithium ion

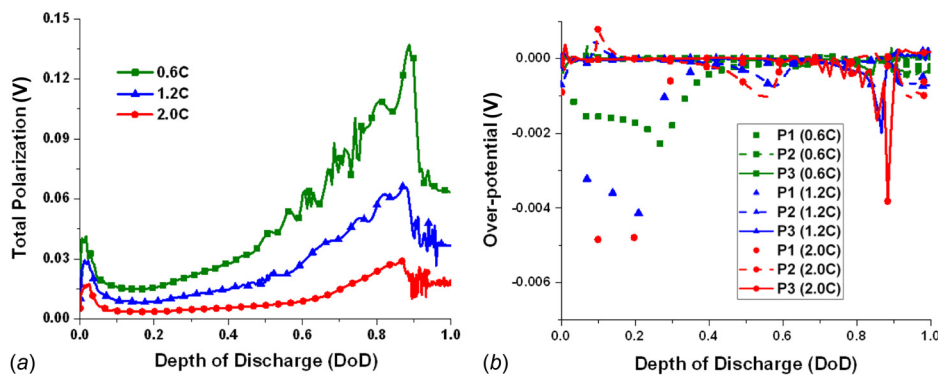


Fig. 5 (a) Total polarization and (b) overpotential at the interface between the electrode and the electrolyte at different points under 0.6 C, 1.2 C, and 2.0 C

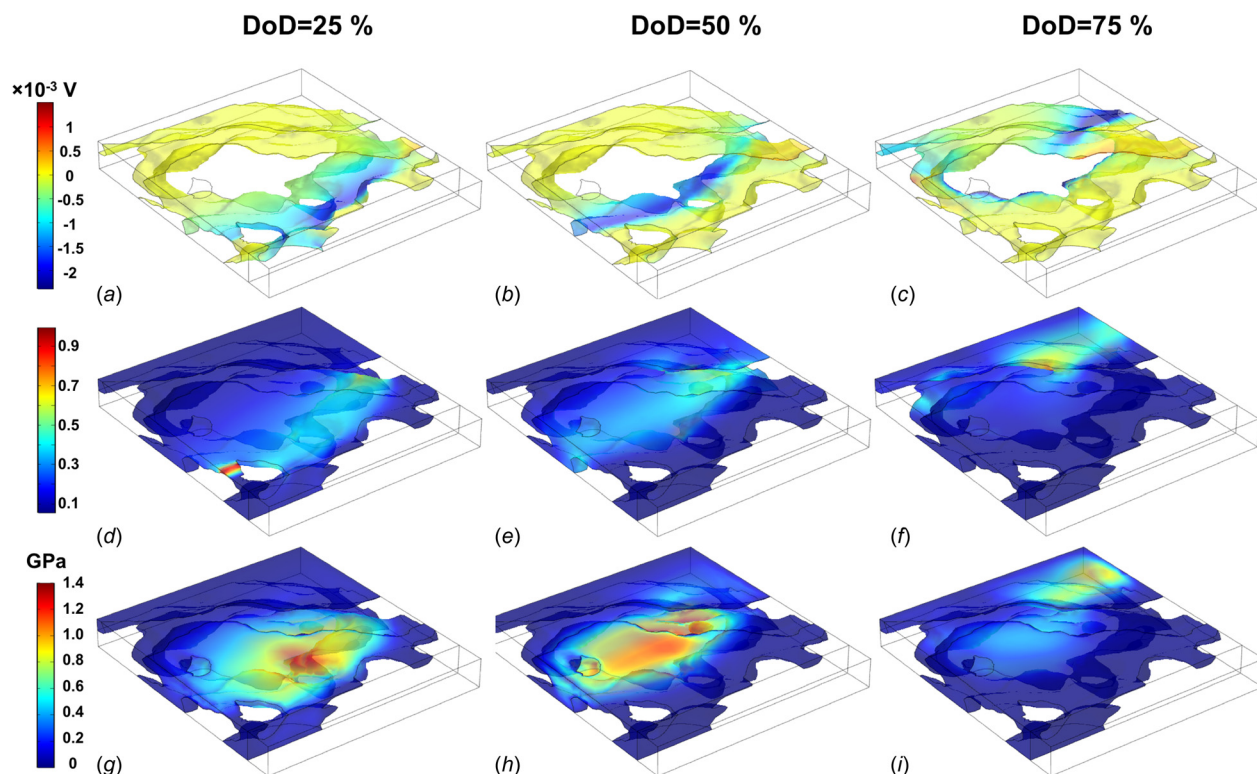


Fig. 6 ((a)–(c)) Contour plots of overpotential at the interface at different DoDs. ((d)–(f)) Contour plots of normalized concentration gradient at different DoDs. ((g)–(i)) Contour plots of von Mises stress distribution at different DoDs. *C*-rate = 0.6 C.

distribution across the electrode, whereas lower *C*-rate discharging produces a relatively more homogeneous lithium ion distribution (Fig. 4).

Figure 5(a) demonstrated total polarization variation during the discharging process under different *C*-rates. We noted two total polarization peaks in Fig. 5(a): the first peak and second peak occurred at the beginning and at the later stages of discharging, respectively. It was concluded that the activation polarization had caused the first peak. That is, the activation polarization was mainly caused by the additional energy during lithium intercalation onto the surface, which was essential to overcome the energy barrier between the electrode and the electrolyte. The activation energy was also measured by the overpotential as shown in Fig. 5(b). Higher overpotential at P_1 under three *C*-rates was also observed at the beginning of discharging. However, the total polarization reached the maximum values at $\text{DoD}=0.86$ for all *C*-rates (Fig. 5(a)). The largest total polarization at the end of discharging was mainly caused by the lithium ion concentration polarization (i.e., the second peak). As shown in Fig. 3(e), most regions of the cathode had reached the maximum concentration prior to $\text{DoD}=0.86$ (at 5400 s), which is when the exchange current density dramatically decreased. This phenomenon could also be verified by Eq. (f) in Table 1, where the decreased exchange current density resulted in limited mass transport in the electrode and correspondingly higher polarization occurred. The results indicate that lithium ion concentration polarization was much higher than the activation polarization during the whole discharging process. Moreover, higher temperature gradients observed at the early stage and at the end of discharging process, as compared to our previous work [2], can also be explained by Fig. 5(a) in the current study, where higher total polarization and higher temperature gradients occurred at the same DoD (i.e., 0.86). Figure 5(b) provided over-potential evolutions for P_1 , P_2 , and P_3 during discharging. Higher overpotential was observed under higher *C*-rate at all points (shown in red). Moreover, for all *C*-rates, P_1 , P_2 , and P_3 showed higher overpotential around $\text{DoD}=0.2, 0.55,$ and $0.85,$

respectively. The results also suggested that lithium intercalation causes higher overpotential at specific DoDs (i.e., 0.2, 0.55, and 0.85). A detailed overpotential distribution is shown in Figs. 6(a)–6(c).

Figure 6 shows the normalized concentration gradient, overpotential, and von Mises stress distribution across the electrode at different DoDs (i.e., 0.25, 0.5, and 0.75) at 0.6 C. In Fig. 6(d), an extremely high concentration gradient was observed in the connecting area near the separator. It was caused by the larger surface area exposed to electrolyte as compared to other regions. In spite of higher concentration gradients at this area, the von Mises stress did not show a significantly higher value. Rather, higher von Mises stress was observed in the center of the particle. From Fig. 6(h), stresses were accumulated inside the particle and were released as discharging proceeded, as shown in Fig. 6(i). Figure 6 suggests that the highest von Mises stress was consistently observed at the same location where the highest normalized concentration gradient and overpotential occurred, except in the connecting area between the particles. This can be explained by the fact that the overpotential and diffusion induced stress both have direct relations to the concentration. It suggested a strong coupling between the mechanical behavior and diffusion in the electrode.

Figure 7 shows the maximum von Mises stress evolution across the cathode during discharging at different *C*-rates. As expected, higher stress was observed at higher *C*-rates. Moreover, as *C*-rate decreased, von Mises stress variation was less significant except at the very beginning and the end of discharging. In other words, the von Mises stress plateaus observed at 0.2 C and 0.6 C, and the plateau region became narrower as *C*-rate increased. For example, at 0.2 C, plateaus were observed between $\text{DoD}=0.2$ and $\text{DoD}=0.8$, but no plateaus were observed at 1.2 C and 2.0 C. Moreover, under high *C*-rate (i.e., 2.0 C), von Mises stress drastically increased from the early stage of discharging until $\text{DoD}=0.5$. A similar trend was also reported in LiCoO_2 by Mendoza et al. [12]. Additionally, Fig. 7 showed that with higher *C*-rate, the maximum stress occurred earlier in the discharging

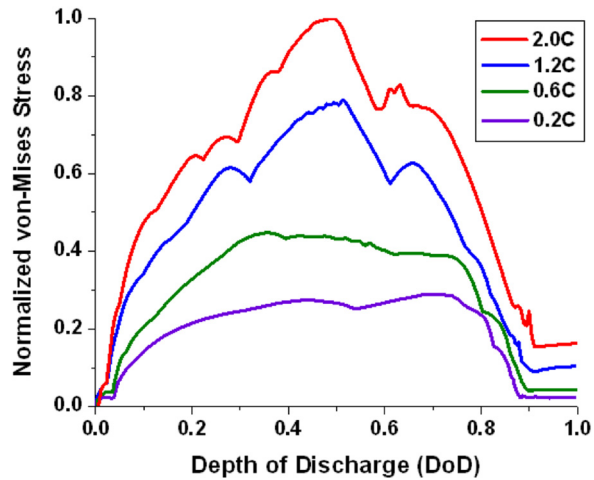


Fig. 7 Maximum normalized von Mises stress variation during discharging at 0.2 C, 0.6 C, 1.2 C, and 2.0 C

process (i.e., at lower DoD). Figure 7 also shows that the normalized maximum von Mises stresses were 0.29, 0.45, 0.79, and 1.0 for 0.2 C, 0.6 C, 1.2 C, and 2.0 C, respectively. In the previous study with core-shell models for cathode materials, it was reported that peak stresses generally occurred when the surface concentration reached saturation [20]. However, the model with 3D reconstructed microstructure in the current study demonstrates that there was no direct relationship between mechanical stress and surface saturation. As shown in Fig. 4, we observed that the surface of the whole electrode was saturated around a depth of discharge of 0.9 for all C-rates. However, the mechanical stress variation after the depth of discharge of 0.9 was not significant. When the cathode surface was fully saturated, the inside of the particle was not fully lithiated at the end of the discharging process (Fig. 3(f)). Thus, we concluded that the mechanical effect of lithium intercalation at the cathode-electrolyte interface was a critical factor, as compared to the mechanical stress due to lithium diffusion inside cathode materials.

4 Conclusions

This study was motivated by the fact that stress-induced fractures can degrade the performance of lithium ion cells. To reveal the relationship between diffusion-induced stress and electrochemical degradation, we developed a three-dimensional finite element model incorporating 3D electrochemical and mechanical analysis in COMSOL MULTIPHYSICS. The microstructure of LiFePO_4 was reconstructed based on a 2D FIB-SEM technique. The multiphysics models developed in this study demonstrated 88.3% of capacity fade at 2 C, which may be explained by higher concentration gradients as compared to lower C-rates. The concentration distribution in the cathode was also presented, and it provided insight toward microstructural effects on electrochemical phenomena. Further, the peak total polarization under each C-rate was observed at the DoD where the higher temperature gradient had also been observed in our previous experiment. At different locations, one of the critical degradation factors (overpotential) indicated that lithium intercalation at the electrode-electrolyte interface causes higher overpotential at specific DoDs. From the maximum normalized von Mises stress variation, higher C-rates showed peak stress, whereas lower C-rates showed stress plateaus within a specific range of DoDs. Finally, the regions where higher mechanical stress was observed were consistent with the regions where higher overpotential and higher concentration gradients also occurred. We believe that our results may be helpful for understanding particle crack initiation in cathode materials.

Further work extending this study should include mechanical interactions between adjacent particles by including carbon black and PVDF binder in a larger region of interest. Specifically, a modified Butler-Volmer equation for electrochemical kinetics, which accounts for the influence of mechanical stress resulting from electrochemical reactions, will be adopted. It will clearly reveal whether there is a direct relationship between electrochemical degradations and mechanical stresses. Moreover, since the anode, made of materials such as silicon or graphite, showed significantly larger volume expansion during electrochemical cycling, a model combining the anode and cathode based on 3D reconstruction will be investigated. We believe it will provide better insight into mechanical stresses in lithium ion cells.

Nomenclature

a, c, l	= anode, cathode, electrolyte
C	= concentration
D	= diffusivity
E_{eq}	= equilibrium potential
F	= Faraday constant
J	= Li ion flux
k	= reaction rate constant
R	= gas constant
ref	= reference
T	= temperature
t_+	= transport number
α	= charge transfer coefficients
η	= overpotential
σ	= ionic conductivity
ϕ	= potential
$\frac{\partial \ln f}{\partial \ln c_i}$	= activity dependence

References

- Palacin, M. R., and De Guibert, A., 2016, "Why Do Batteries Fail?," *Science*, **351**(6273), pp. 574–581.
- Kim, S., and Huang, H.-Y. S., 2016, "Mechanical Stresses at the Cathode-Electrolyte Interface in Lithium-Ion Batteries," *J. Mater. Res.*, **31**(22), pp. 3506–3512.
- Kim, S., Wee, J., Peters, K., and Huang, H.-Y. S., 2018, "Multiphysics Coupling in Lithium-Ion Batteries With Reconstructed Porous Microstructures," *J. Phys. Chem. C*, **122**(10), pp. 5280–5290.
- Xu, R., and Zhao, K., 2016, "Mechanical Interactions Regulated Kinetics and Morphology of Composite Electrodes in Li-Ion Batteries," *Extrem. Mech. Lett.*, **8**, pp. 13–21.
- Lu, B., Song, Y., Zhang, Q., Pan, J., Cheng, Y.-T., and Zhang, J., 2016, "Voltage Hysteresis of Lithium Ion Batteries Caused by Mechanical Stress," *Phys. Chem. Chem. Phys.*, **18**(6), pp. 4721–4727.
- Mendoza, H., Roberts, S. A., Brunini, V. E., and Grillet, A. M., 2016, "Mechanical and Electrochemical Response of a LiCoO_2 Cathode Using Reconstructed Microstructures," *Electrochim. Acta*, **190**, pp. 1–15.
- Ghorbani Kashkooli, A., Foreman, E., Farhad, S., Lee, D. U., Ahn, W., Feng, K., De Andrade, V., and Chen, Z., 2017, "Synchrotron X-Ray Nano Computed Tomography Based Simulation of Stress Evolution in LiMn_2O_4 electrodes," *Electrochim. Acta*, **247**, pp. 1103–1116.
- Liu, Z., Chen-Wiegart, Y. K., Wang, J., Barnett, S. A., and Faber, K. T., 2016, "Three-Phase 3D Reconstruction of a LiCoO_2 Cathode Via FIB-SEM Tomography," *Microsc. Microanal.*, **22**(1), pp. 140–148.
- Biton, M., Yufit, V., Tariq, F., Kishimoto, M., and Brandon, N., 2017, "Enhanced Imaging of Lithium Ion Battery Electrode Materials," *J. Electrochem. Soc.*, **164**(1), pp. 6032–6038.
- Ender, M., Joos, J., Carraro, T., and Ivers-Tiffée, E., 2012, "Quantitative Characterization of LiFePO_4 Cathodes Reconstructed by FIB/SEM Tomography," *J. Electrochem. Soc.*, **159**(7), pp. A972–A980.
- Scipioni, R., Jorgensen, P. S., Ngo, D.-T., Simonsen, S. B., Liu, Z., Yakal-Kremiski, K. J., Wang, H., Hjelm, J., Norby, P., Barnett, S. A., and Jensen, S. H., 2016, "Electron Microscopy Investigations of Changes in Morphology and Conductivity of LiFePO_4/C Electrodes," *J. Power Sources*, **307**, pp. 259–269.
- Kashkooli, A. G., Farhad, S., Lee, D. U., Feng, K., Litster, S., Babu, S. K., Zhu, L., and Chen, Z., 2016, "Multiscale Modeling of Lithium-Ion Battery Electrodes Based on Nano-Scale X-Ray Computed Tomography," *J. Power Sources*, **307**, pp. 496–509.
- Christensen, J., 2010, "Modeling Diffusion-Induced Stress in Li-Ion Cells With Porous Electrodes," *J. Electrochem. Soc.*, **157**(3), pp. A366–A380.
- Tahmasebi, A., Sedaghat, A., Kalbasi, R., and Zand, M. M., 2013, "Performance Assessment of a Hybrid Fuel Cell and Micro Gas Turbine Power System," *Energy Equip. Syst.*, **1**, pp. 59–74.

- [15] Kim, S., 2015, "Stresses at Electrode-Electrolyte Interface in Lithium-Ion Batteries Via Multiphysics Modeling," *M.S. thesis*, North Carolina State University, Raleigh, NC.
- [16] Zhu, M., Park, J., and Sastry, A. M., 2012, "Fracture Analysis of the Cathode in Li-Ion Batteries: A Simulation Study," *J. Electrochem. Soc.*, **159**(4), pp. A492–A498.
- [17] Xu, R., Scalco De Vasconcelos, L., and Zhao, K., 2016, "Computational Analysis of Chemomechanical Behaviors of Composite Electrodes in Li-Ion Batteries," *J. Mater. Res.*, **31**(18), pp. 2715–2727.
- [18] ChiuHuang, C.-K., and Huang, H.-Y. S., 2015, "Critical Lithiation for C-Rate Dependent Mechanical Stresses in LiFePO_4 ," *J. Solid State Electrochem.*, **19**(8), pp. 2245–2253.
- [19] ChiuHuang, C.-K., and Shadow Huang, H.-Y., 2013, "Stress Evolution on the Phase Boundary in LiFePO_4 Particles," *J. Electrochem. Soc.*, **160**(11), pp. A2184–A2188.
- [20] Maxisch, T., and Ceder, G., 2006, "Elastic Properties of Olivine Li_xFePO_4 From First Principles," *Phys. Rev. B*, **73**(17), p. 174112.